Monthly Notices of the ROYAL ASTRONOMICAL SOCIETY

MNRAS **521,** 3247–3259 (2023) https://doi.org/10.1093/mnras/stad774
Advance Access publication 2023 March 17

The connection between the escape of ionizing radiation and galaxy properties at $z \sim 3$ in the Keck Lyman continuum spectroscopic survey

Anthony J. Pahl [1]★ Alice Shapley,[1] Charles C. Steidel,[2] Naveen A. Reddy,[3] Yuguang Chen [2,4] Gwen C. Rudie[5] and Allison L. Strom[6]

[1]*Department of Physics and Astronomy, University of California, Los Angeles, CA 90095, USA*
[2]*Cahill Center for Astronomy and Astrophysics, California Institute of Technology, MC249-17, Pasadena, CA 91125, USA*
[3]*Department of Physics and Astronomy, University of California Riverside, Riverside, CA 92521, USA*
[4]*Department of Physics and Astronomy, University of California Davis, 1 Shields Avenue, Davis, CA 95616, USA*
[5]*The Observatories of the Carnegie Institution for Science, 813 Santa Barbara Street, Pasadena, CA 91101, USA*
[6]*Center for Interdisciplinary Exploration & Research in Astrophysics (CIERA) and Department of Physics & Astronomy, Northwestern University, Evanston, IL, 60208, USA*

Accepted 2023 March 6. Received 2023 February 9; in original form 2022 October 30

ABSTRACT

The connection between the escape fraction of ionizing radiation (f_{esc}) and the properties of galaxies, such as stellar mass (M_*), age, star-formation rate (SFR), and dust content, are key inputs for reionization models, but many of these relationships remain untested at high redshift. We present an analysis of a sample of 96 $z \sim 3$ galaxies from the Keck Lyman Continuum Spectroscopic Survey (KLCS). These galaxies have both sensitive Keck/LRIS spectroscopic measurements of the Lyman continuum (LyC) region, and multiband photometry that places constraints on stellar population parameters. We construct composite spectra from subsamples binned as a function of galaxy property and quantify the ionizing-photon escape for each composite. We find a significant anti-correlation between f_{esc} and M_*, consistent with predictions from cosmological zoom-in simulations. We also find significant anti-correlation between f_{esc} and $E(B-V)$, encoding the underlying physics of LyC escape in our sample. We also find no significant correlation between f_{esc} and either stellar age or specific SFR ($=$ SFR/M_*), challenging interpretations that synchronize recent star formation and favorable conditions for ionizing escape. The galaxy properties now shown to correlate with f_{esc} in the KLCS are Lyα equivalent width, UV Luminosity, M_*, SFR, and $E(B-V)$, but not age or sSFR. This comprehensive analysis of galaxy properties and LyC escape at high redshift will be used to guide future models and observations of the reionization epoch.

Key words: galaxies: high-redshift – cosmology: observations – dark ages, reionization, first stars.

1 INTRODUCTION

Reionization is a significant phase transition in the Universe, during which hydrogen in the intergalactic medium (IGM) transitions from neutral to ionized. This transformation appears to end at $z \sim 6$ (Fan, Carilli & Keating 2006), but we still lack a comprehensive description of the physical processes responsible for the reionization history. At $z > 6$, the ionizing background of the Universe is thought to be dominated by ionizing photons produced by O/B stars in star-forming galaxies (Bouwens et al. 2015; Parsa, Dunlop & McLure 2018). Different models of reionization attempt to use integrated measurements of galaxy populations and independent constraints on the IGM hydrogen neutral fraction to infer the comprehensive evolution of reionization from the early Universe to $z \sim 6$, but can arrive at remarkably different answers. Reionization may start 'late,' such that neutral fractions remain at $\gtrsim 90$ per cent until $z \sim 8$ (e.g. Naidu et al. 2020), or reionization may be 'gradual,' such that the neutral fraction decreases slowly from $z \sim 12$ until $z \sim 6$ (e.g. Finkelstein et al. 2019).

To draw conclusions about the evolution of the neutral fraction from observations of galaxies, one must attempt to understand the ionizing emissivity of galaxies as a function of cosmic time. This quantity is commonly parametrized as a function of three variables: the UV luminosity function (ρ_{UV}), the ionizing photon production efficiency (ξ_{ion}), and the fraction of ionizing luminosity that escapes the interstellar and circumgalactic medium (ISM and CGM) and proceed to ionize the IGM (f_{esc}) (Robertson et al. 2015). While constraints are available for both ρ_{UV} and ξ_{ion} well into the epoch of reionization (Madau & Dickinson 2014; Stark et al. 2015, 2017), f_{esc} is uniquely difficult to ascertain in the early Universe. Estimating f_{esc} requires direct observations of the ionizing radiation from galaxies in the Lyman continuum (LyC) spectral region. The transmission through the general IGM of LyC photons escaping a galaxy depends sensitively on emission redshift and decreases rapidly beyond $z \sim 3.5$ (Vanzella et al. 2012). This drop off is due to LyC absorption from trace amounts of H I and makes direct determinations of f_{esc} impossible during the epoch of reionization itself.

★ E-mail: pahl@astro.ucla.edu

Models of reionization are distinguished by their assumptions about f_{esc}. Finkelstein et al. (2019) present a 'democratic' model for reionization that assumes that the process is driven by faint sources with high f_{esc} values. In contrast, the 'oligarchical' model of Naidu et al. (2020) concludes that massive luminous ($M_{UV} < -18$ and $\log(M_*/M_\odot) > 8$) galaxies provide the bulk of ionizing photons during reionization. For testing assumptions of f_{esc} during reionization, $z \sim 3$–4 galaxies provide an essential laboratory, and can discern the fundamental properties that govern f_{esc} at the highest redshifts these measurements can be made. Critically, these galaxies may be closer analogues to reionization era galaxies than those in the local Universe (e.g. Flury et al. 2022a, b).

A number of LyC observational surveys at $z \sim 3$–4 have attempted to measure average f_{esc} values and potential correlations between f_{esc} and the properties of galaxies. Success has been found by stacking deep observations of the LyC either photometrically (e.g. Begley et al. 2022) or spectroscopically (Marchi et al. 2017). Here, we focus on the Keck Lyman Spectroscopic (KLCS) survey, which included deep Keck/Low Resolution Imaging Spectrometer (LRIS; Oke et al. 1995; Steidel et al. 2004) spectra of Lyman break galaxies (LBGs) at $z \sim 3$ (Steidel et al. 2018). Steidel et al. (2018) reported an average $f_{esc} = 0.09 \pm 0.01$ from 124 LBGs, estimated by stacking their rest-UV spectra with coverage of the LyC region. After careful treatment of line-of-sight contamination using *HST* imaging, the average KLCS f_{esc} was corrected to 0.06 ± 0.01 upon removal of four apparently contaminated galaxies from the sample (Pahl et al. 2021). This significant reduction in sample-averaged f_{esc} highlights the importance of foreground decontamination in studies of LyC at high redshift. Galaxy properties correlated with inferred f_{esc} in the KLCS are determined to be Ly α equivalent width (W_λ(Lyα)) and UV luminosity (L_{UV}), such that galaxies with stronger Ly α emission and lower L_{UV} luminosities tend to have higher f_{esc} (Steidel et al. 2018; Pahl et al. 2021). In the 2018 paper, we explained why W_λ(Ly α) is more fundamental in its correlation with f_{esc}, as W_λ(Ly α) is modulated by the neutral gas covering fraction of a galaxy (Reddy et al. 2016b; Gazagnes et al. 2020), which similarly modulates the escape of ionizing radiation. Trends between f_{esc}, W_λ(Ly α), and L_{UV} have also been recovered in complementary LyC surveys at $z \sim 3$ (Marchi et al. 2017, 2018; Begley et al. 2022), but L_{UV} and W_λ(Ly α) ultimately represent a limited parameter space from which to construct a comprehensive picture of LyC escape in star-forming galaxies.

Promising indirect indicators of f_{esc} may surface from the feedback of star formation and its effect on the ISM and CGM of a galaxy. Cosmological zoom-in simulations coupled with radiative transfer calculations indicate that feedback from recent dense star-formation can induce favourable channels in the ISM and CGM that allow ionizing photons to escape (Ma et al. 2020). Understanding f_{esc} as a function of the surface density of star formation (Σ_{SFR}), stellar age, or specific star-formation rate would allow observational comparison to these simulations, and empirically connect the history of star formation to f_{esc}. Additionally, dust attenuation is intricately linked to the neutral gas covering fraction in the ISM and CGM, but the relationship between f_{esc} and $E(B-V)$ at $z \sim 3$ has thus far only been investigated using rest-UV observations (Reddy et al. 2016a, b; Steidel et al. 2018). Thanks to multiband photometry available for the KLCS, which can constrain stellar population parameters, we can explore these relationships at high redshift, many for the first time.

In Pahl et al. (2022), we began by examining 35 galaxies from the KLCS that were covered by *HST* imaging, enabling measurements of rest-UV sizes. Together with SFR estimates from fits to multiband photometry, we measured Σ_{SFR} and attempted to constrain f_{esc} versus Σ_{SFR}. We ultimately determined that the limited KLCS subsample with *HST* imaging was too small and unrepresentative to determine trends with f_{esc} and galaxy property. In the present work, we extend the analysis of Pahl et al. (2022), by examining SED-modelled measurements of stellar mass (M_*), $E(B-V)$, stellar age, and SFR instead, which allow nearly the entire KLCS sample to be utilized. By performing stacking of rest-UV spectra as a function of galaxy property, we investigate the dependence of f_{esc} on these galaxy properties. Significant correlations will test existing reionization models and strongly inform future ones.

We organize the paper as follows: in Section 2, we review the spectroscopic observations of the KLCS sample and its ancillary photometric measurements, and provide an overview of the SED and spectral fitting methodology. In Section 3, we present the SED-modelled parameters for individual galaxies and estimates of ionizing escape from binned subsamples. In Section 4, we explore similar observational analyses from the literature, connections to cosmological zoom-in simulations, and implications for reionization. We summarize our main conclusions in Section 4.3.

Throughout this paper, we adopt a standard ΛCDM cosmology with $\Omega_m = 0.3$, $\Omega_\Lambda = 0.7$ and $H_0 = 70$ km s^{-1}Mpc^{-1}. The f_{esc} values reported in this paper are absolute escape fractions, equivalent to $f_{esc,\,abs}$ in Steidel et al. (2018), and defined as the fraction of all H-ionizing photons produced within a galaxy that escapes into the IGM. We also employ the AB magnitude system (Oke & Gunn 1983).

2 SAMPLE AND METHODOLOGY

In order to understand how ionizing photon escape is tied to measurable characteristics of galaxy stellar populations or the spatial distribution of the interstellar gas, we require integrated photometric measurements that sample a wide wavelength baseline as well as direct constraints on the LyC emission. Both types of measurements are available for KLCS galaxies. In this section, we outline the data included in our analysis, featuring an overview of the KLCS sample, associated spectra, and the multiband photometry available for KLCS galaxies. We explain the methodology of SED fitting to determine galaxy properties and spectral modeling to estimate parametrizations of ionizing-photon escape such as f_{esc}.

2.1 Uncontaminated KLCS

The primary goal of the KLCS was to examine the hydrogen-ionizing spectra of star-forming galaxies at $z \sim 3$ (Steidel et al. 2018). To this end, 137 galaxies were observed with LRIS on the Keck I telescope on Mauna Kea, Hawai'i. Each object was observed for 8.2 h at minimum. These observations began in 2006 and were concluded in 2008. Of 137 targets, 13 galaxies were removed due to either instrumental defects or spectroscopic evidence of contamination by foreground galaxies. The final sample presented in Steidel et al. (2018) numbered 124 galaxies. Of these, 15 galaxies apparently had significant flux density in the LyC spectral region, defined as having $f_{900} > 3\sigma_{900}$, where f_{900} is the average flux density between 880–910 Å in the rest frame, and σ_{900} is the standard deviation of flux densities in the same spectral region. Objects meeting this criteria were defined as individual LyC 'detections,' with the remaining 109 galaxies labelled as LyC 'non-detections.'

Despite the efforts of Steidel et al. (2018) to produce a clean sample of LyC leakers at $z \sim 3$ by looking for evidence of spectral blending, foreground contamination remains a significant concern for surveys of LyC at high redshift (Vanzella et al. 2012; Mostardi et al. 2015). A galaxy along the line of sight to a $z \sim 3$ source

Table 1. Photometric bands used in SED modelling.

Fields	Photometric bands
Q0100	U_n^a, B^a, G^a, R_s^a, J^b, H^b, K_s^c, IRAC1, IRAC2, IRAC3, H_{140}, H_{160}
Q0256	U_n^d, G^d, R_s^d, J^c, K_s^c, IRAC1
B20902	U_n^e, $G^{d,e}$, $R_s^{d,e}$, J^f, K_s^f, IRAC1, IRAC2
Q0933	U_n^d, G^d, R_s^d, I^d, J^c, K_s^c, IRAC1, IRAC2, V_{606}, J_{125}, H_{160}
Q1009	U_n^a, G^a, R_s^a, J^g, K_s^g, IRAC1, H_{140}, H_{160}
Westphal	u*^{h}, g'^{h}, r'^{h}, i'^{h}, z'^{h}, J^i, H^i, $K_s^{i,f}$, IRAC1, IRAC2, V_{606}, J_{125}, H_{160}
Q1422	U_n^e, G^e, R_s^e, K_s^c, IRAC1, IRAC2, V_{606}, J_{125}, H_{160}
Q1549	U_n^a, G^a, R_s^a, J^b, H^b, $K_s^{b,c}$, IRAC1, IRAC2, IRAC3, V_{606}, J_{125}, H_{160}
DSF2237b	U_n^d, G^d, R_s^d, I^d, $J^{c,f}$, $K_s^{c,f}$, IRAC1, IRAC2, V_{606}, J_{125}, H_{160}

[a]Observed with Keck/LRIS. [b]Observed with FourStar at the Magellan Baade 6.5m telescope. [c]Observed with the Multiobject Spectrometer for Infra-Red Exploration (MOSFIRE) on the Keck I telescope. [d]Observed with the COSMIC prime focus imager on the Palomar 5.08 m telescope (see Steidel et al. 2003). [e]Observed with the Prime Focus Imager on the William Herschel 4.2 m telescope (WHT) (see Steidel et al. 2003). [f]Observed with NIRC on the Keck I telescope (Shapley et al. 2001). [g]Observed with the Wide Field Infrared Camera (WIRC) on the Palomar 5.08m telescope. [h]From the Canada–France–Hawaii Telescope (CFHT) Legacy Survey. [i]Observed with CFHT/WIRCam as part of the WIRCam Deep Survey (Bielby et al. 2012).

can provide non-ionizing photons that masquerade as rest-frame LyC assuming a single redshift of $z \sim 3$. As such, Pahl et al. (2021) presented new *HST* measurements of the 15 individual LyC detections in the KLCS sample, which were the objects most likely to be significantly contaminated by foreground light. These data were taken across five survey fields, including seven ACS/F606W (V_{606}) pointings and 11 WFC3/F125W (J_{125}), and WFC3/F160W (H_{160}) pointings. Each pointing was observed for three orbits in each filter. Pahl et al. (2021) also utilized existing *HST* data for one object (Q1549-C25) from Mostardi et al. (2015) and Shapley et al. (2016). Based on the $V_{606}J_{125}H_{160}$ colours of the subcomponents in the high resolution, *HST* light profiles, two individual LyC detections were determined to be likely contaminated. An additional 24 LyC non-detections were included in the aforementioned *HST* pointings and were also analysed. Two of these were found to have associated subcomponents with colours consistent with foreground sources. In total, four galaxies were removed from the KLCS, for a final sample size of 120, including 13 galaxies individually detected in LyC.

2.2 Photometry and SED fits

Several galaxy properties can be estimated from broad-band photometric measurements. In addition to the U_nGR images used for original photometric selection of $z \sim 3$ candidates (see Steidel et al. 2003), longer wavelength photometry of the KLCS has been obtained. We summarize the photometric information available for the objects in KLCS in Table 1. A subset of these measurements are also summarized and analysed in Pahl et al. (2022). Specifically, optical, near-IR, and mid-IR data were available for the majority of galaxies in KLCS. We required at least one photometric measurement entirely redward of the Balmer break in order to accurately constrain the stellar populations. The filters that fulfilled this requirement for the KLCS were the H, K_s, and Spitzer/IRAC bands. Thirteen objects do not have sufficient IR measurements (i.e. did not have any photometric measurements entirely redward of the Balmer break) and were removed from our sample. In addition, we removed two objects with significant scattered light in their ground-based light profiles from nearby objects, and one galaxy identified with multiple redshifts in the original KLCS spectrum.

HST photometry was included for the 35 objects observed in the *HST* $V_{606}J_{125}H_{160}$ pointings presented in Pahl et al. (2021). In addition to these 35 objects, 11 objects were covered by at least one *HST* filter, without the full $V_{606}J_{125}H_{160}$ data set required for contamination analysis. *HST* H_{160} imaging was also available for four objects in the Q0100 field and two objects in Q1009 (Law et al. 2012). We remeasured integrated photometry for all objects in KLCS with $V_{606}J_{125}H_{160}$ *HST* data available largely following the methodology of Pahl et al. (2021, 2022). In an effort to improve consistency between all photometric measurements, we adopted *HST* magnitudes from the same MAG_AUTO parameter from SEXTRACTOR (Bertin & Arnouts 1996) that was employed by the ground-based measurements, rather than the isophotal *HST* magnitudes adopted by Pahl et al. (2021, 2022). Finally, we note that *HST* H_{140} measurements are available for three objects in Q0100 and five in Q1009, which were included in our analysis (Chen et al. 2021).

We attempted to correct the photometry from potential biases resulting from strong emission lines that lie in the bandpass of individual filters. Notably, we used existing Keck/MOSFIRE spectra with coverage of [O II]$\lambda\lambda$3726, 3729, Hβ, and [O III]$\lambda\lambda$4959, 5007 rest-optical lines to correct broad-band H and K_s flux measurements, depending on the wavelength of the observed line. We identified eight objects with neither Keck/MOSFIRE spectra nor additional photometry redward of the Balmer break aside from H or K_s. We removed these objects from the sample to ensure all galaxies in our analysis had at least one trustworthy photometric measurement redward of the Balmer break, free of potential emission-line bias. In addition, we used Lyα equivalent widths presented in Steidel et al. (2018) to correct broadband G and V_{606} flux measurements if the observed wavelength of the line was contained in the respective bandpass.

The final sample with sufficient multiband photometry for robust stellar population modelling consisted of 96 galaxies, of which 12 were individual LyC detections, which we define as the 'KLCS SED' sample. In Fig. 1, we display the KLCS SED sample as a function of key observables from Steidel et al. (2018), including spectroscopic redshift z_{sys}, Lyα equivalent width W_λ(Lyα), and UV luminosity (L_{UV}/L^*_{UV}, where the characteristic luminosity L^*_{UV} corresponds to $M^*_{UV} = -21.0$). We simultaneously present the characteristics of the parent KLCS sample of 120 galaxies. Median z_{sys}, L_{UV}, and W_λ(Lyα) values for KLCS SED are consistent with those for the full KLCS sample.

In order to estimate stellar-population parameters such as stellar mass (M_*), star-formation rate (SFR), stellar age, and $E(B-V)$ for

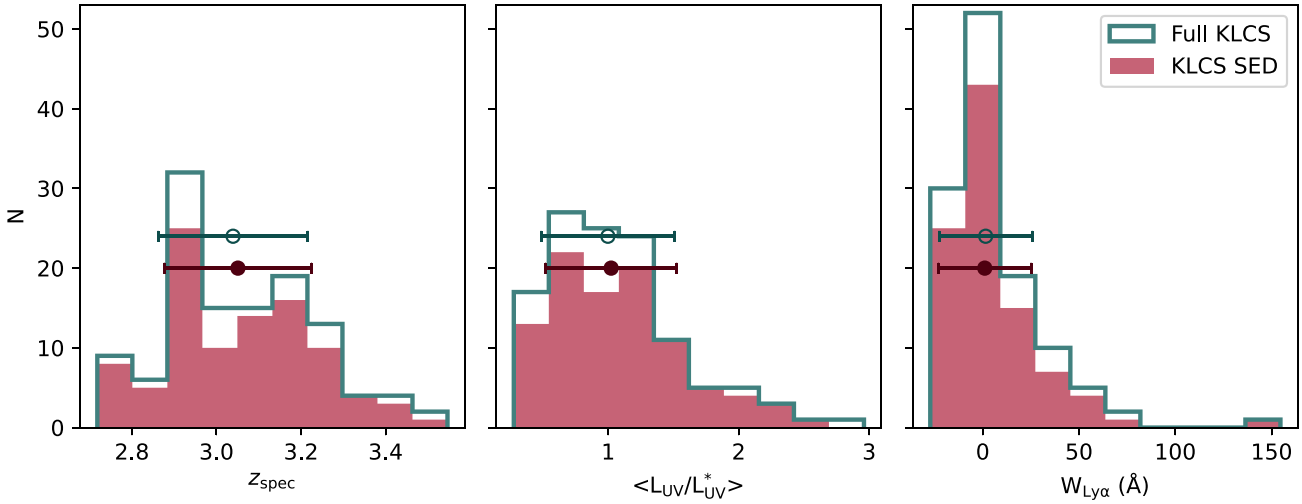

Figure 1. Distributions of z_{spec}, L_{UV}, and $W_\lambda(\mathrm{Ly}\,\alpha)$ for the KLCS SED sample and the full KLCS. The full KLCS sample includes 120 galaxies from Pahl et al. (2021) while the KLCS SED sample contains the 96 galaxies with photometry appropriate for SED fitting. The median and standard deviation of each distribution are presented respectively as single data points and error bars. The filled circle is the sample median of the KLCS SED sample while the open circle is the sample median of the full KLCS.

the galaxies in the KLCS SED sample, we employed SED fits to the multiband photometry available for these objects. We broadly followed the fitting methodology of Reddy et al. (2022) (also see Pahl et al. 2022). In brief, we utilized BPASS stellar-population synthesis models (BPASS v2.2.1; Eldridge et al. 2017) assuming a Chabrier (2003) initial-mass function. We assumed a constant star-formation history (SFH) with stellar population ages greater than 50 Myr, such that stellar ages would not be less than typical dynamical-time-scales of $z \sim 3$ star-forming galaxies (Reddy et al. 2012). We adopted constant SFHs as they have been shown to reproduce independent measurements of SFR for galaxies $z \geq 1.5$ (Reddy et al. 2012). Constant SFHs may also provide a better description of galaxies at the stellar masses of our sample ($\sim 10^9$–$10^{10.5}$ $\mathrm{M}_\odot$), which may have less bursty SFHs than galaxies at lower masses (e.g. Domínguez et al. 2015). We adopted assumptions of metallicity of 0.14 times solar and an SMC dust attenuation curve (Gordon et al. 2003). We examined each SED fit individually for outlier photometric measurements, and dropped Spitzer/IRAC data with clear evidence of blending from nearby sources. Given our SED fitting methodology, we note that galaxies fit with larger masses tended to have higher SFRs and stellar ages. Over the mass range of our sample, we do not find a significant trend with M_* and $E(B-V)$, which may be expected considering the weak relationship that has been recovered between M_* and $E(B-V)$ when assuming the SMC dust extinction curve in the interpretation of galaxy colours vs. M_* SED (McLure et al. 2018).

2.3 Binning strategy and spectral modelling

While f_{900} can be measured for each object individually, constraining the LyC leaking in the vicinity of a galaxy requires an understanding of the attenuation of the signal from neutral hydrogen along the line of sight in the IGM and CGM. The transmission of LyC emission varies significantly from sightline to sightline at the redshifts of our sample, introducing large uncertainties on individual LyC measurements (Steidel et al. 2018). To circumvent this sightline to sightline variability, we used binned subsamples and composite spectra that reflect average effects of IGM and CGM attenuation on the LyC spectral region as in Steidel et al. (2018). In order to understand how ionizing-spectral properties vary with the properties produced by SED fits described in the previous section, we binned the KLCS SED sample as a function of M_*, SFR, $E(B-V)$, age, and specific star-formation rate (sSFR; $\mathrm{sSFR} \equiv \mathrm{SFR}/\mathrm{M}_*$). We created three bins for each property, each containing 32 galaxies, to ensure that the mean IGM + CGM transmission is known with $\lessapprox 10$ per cent uncertainty (Steidel et al. 2018) in subsequent composite spectra. We also created an 'all' sample, containing all 96 galaxies from KLCS SED, and binned subsamples for $W_\lambda(\mathrm{Ly}\,\alpha)$ and L_{UV}.

For each subsample, we generated composite spectra representing the average spectral properties of the component galaxies. Following the methodology of Steidel et al. (2018) (also see Pahl et al. 2021, 2022), each individual spectrum is first normalized to the average flux density in the non-ionizing UV spectral region, 1475–1525 Å in the rest frame. Using the set of normalized spectra for each binned sample, we then computed the sigma-clipped mean of the distribution of flux densities at each rest-frame wavelength increment, with clipping applied at 3σ. We did not apply sigma clipping to the Ly α spectral region (1200−1230 Å) in order to conserve the inferred composite Ly α profile. The error on the mean flux density at each wavelength was propagated from the values of individual error spectra.

For each composite spectrum, we computed $\langle f_{900}/f_{1500}\rangle_{\mathrm{obs}}$, which is the ratio between the average flux densities in the LyC region (880–910 Å, f_{900}) and the non-ionizing UV continuum (1475–1525 Å, f_{1500}). While this ratio is useful for discerning the average observed ionizing photon leakage relative to the non-ionizing ultraviolet luminosity density, as discussed above, the spectra must be corrected for lowered transmission from the IGM in the LyC region in order to understand the average effect of LyC leakage has on its environment. We corrected the spectra using average 'IGM + CGM' transmission functions from Steidel et al. (2018), calculated at the mean redshift of each composite subsample, and based on the statistics of H I absorption systems along QSO sightlines presented by Rudie et al. (2012, 2013). To demonstrate the characteristics of the composite spectra used in our analysis, we display the 'all' composite before and after the IGM + CGM transmission correction in the upper panel of Fig. 2. Using corrected spectra, we repeated the measurement of the ratio of f_{900} to f_{1500}, defined as $\langle f_{900}/f_{1500}\rangle_{\mathrm{out}}$, which applies to the

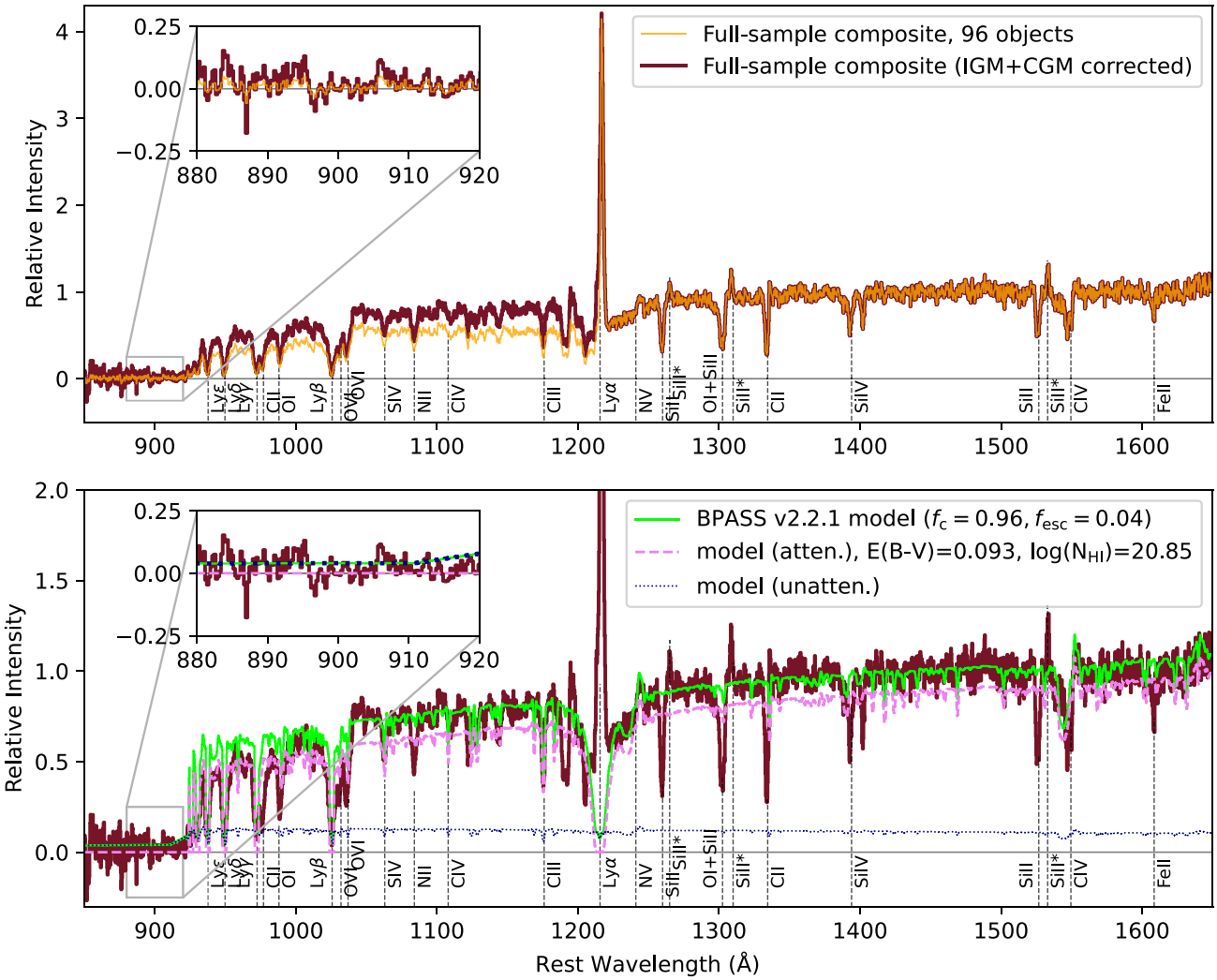

Figure 2. Composite spectrum for the 'all' (full KLCS SED, 96 galaxy) sample. **Top:** The 'all' composite alongside the same spectrum corrected from the average attenuation from the IGM and CGM at the mean redshift of the composite, $z_{mean} = 3.05$. The uncorrected spectrum is shown with a thin, orange curve, while the corrected composite is shown with a thick, maroon curve. An inset is included to highlight the LyC spectral region. **Bottom:** IGM- and CGM-corrected composite spectrum alongside the best-fitting spectrum from the modelling process. The corrected composite is again shown with the thick, maroon curve. The best-fitting BPASS model is presented as a thin green curve. This model is summed from two component spectra, an attenuated portion displayed as a dashed pink line, and an unattenuated portion displayed as a dotted blue line, as per the 'holes' model of Steidel et al. (2018). An inset is included to highlight the LyC spectral region. The free parameters values of the fit that produced the model curves are $f_c = 0.96$, $E(B-V)$=0.093, and $\log(N_{HI}/cm^{-2}) = 20.85$.

ratio that would be observed at 50 proper kpc from galaxy centre (see Steidel et al. 2018).

While $\langle f_{900}/f_{1500}\rangle_{out}$ is a useful empirical measurement of leaking LyC, f_{esc} remains extensively used in reionization modelling. In order to calculate the average f_{esc} for each subsample, we require both an understanding of the intrinsic UV spectrum of the galaxies and the average effects from any intervening gas in the ISM. Thus, f_{esc} is dependent on the assumed stellar population synthesis model, and we follow the well-motivated choices for such models discussed in Steidel et al. (2018). We introduced consistency between our multiwavelength and spectroscopic modeling by again using the BPASS stellar-population synthesis models of Eldridge et al. (2017). We coupled these models with an SMC extinction curve (Gordon et al. 2003) and a range of $E(B–V)$ from 0.0 to 0.6, and assumptions of metallicity of 0.07 times solar. This metallicity is similar to that assumed for the SED fitting and is consistent with the spectral modelling of Steidel et al. (2018) and Pahl et al. (2021). We model the ISM geometrically using the 'holes' approach, which assumes LyC light escapes through a patchy neutral-phase gas (Zackrisson, Inoue & Jensen 2013; Reddy et al. 2016b, 2022). The free parameters of the fit included the neutral gas covering fraction f_c, the column density of neutral hydrogen N_{HI}, and the dust attenuation from the foreground gas $E(B-V)_{cov}$ (i.e. the uncorrected portion is assumed to be dust free). In general, f_{esc} is defined from f_c, where $f_{esc} = 1 - f_c$. To demonstrate the fitting process, we display a fit to the corrected full-sample composite in the lower panel of Fig. 2. Here, the modelled spectrum in green is split into an unattenuated (blue) and attenuated (pink) portion, representing the light that either escaped through clear sightlines in the ISM or was partially reduced by intervening material, respectively.

In order to estimate the uncertainty in average escape parameters for a given set of galaxies, we must understand the level of variability induced from sample construction, while simultaneously including the uncertainty on galaxy property measurements. We perturbed each

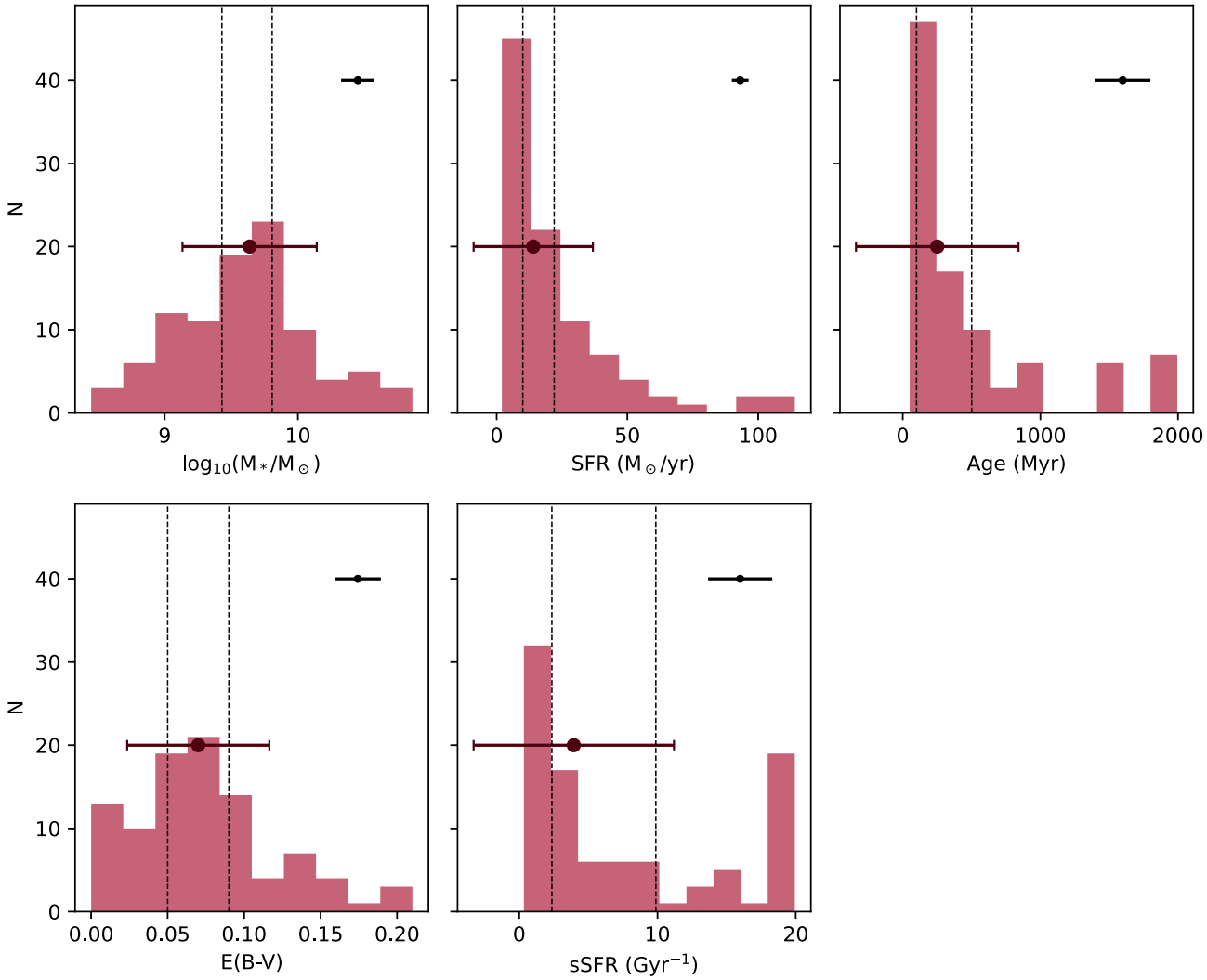

Figure 3. Galaxy property distributions of the KLCS SED sample. The five properties displayed here were inferred from SED fits performed for each galaxy. The median and standard deviations with respect to a given measurement are presented as large data points with capped error bars, while the typical (median) error on individual measurements are presented as smaller data points in the upper left with uncapped error bars. The edges of bins used for generation of composite spectra are shown as vertical dashed lines. The full sample was sorted according to each galaxy property and divided into three equal-sized bins (n = 32), which were then used to generate composite spectra.

individual measurement randomly by a Gaussian characterized by a width equal to its error, and constructed 100 modified parameter histograms for each galaxy property. We then binned each perturbed sample distribution into three subsamples of increasing galaxy property, with 32 galaxies in each subsample. Finally, with the goal of understanding how sample variance affects generated composite spectra, we used bootstrap resampling of the galaxies of each binned subsample. For each of the 100 sets of 32 galaxies (generated from the modified parameter distributions), we drew one new subsample with replacement. We subsequently created composite spectra and measured ionizing-photon escape for each random draw, using the process described earlier in this section. The mean and standard deviation of the $\langle f_{900}/f_{1500}\rangle_{\rm obs}$, $\langle f_{900}/f_{1500}\rangle_{\rm out}$, and $f_{\rm esc}$ distributions generated from the 100 composite spectra were used as the fiducial value and error estimate for the corresponding binned sample. The errors determined from this bootstrap resampling were larger than those associated with measurement uncertainty, average IGM + CGM transmission variability, and errors from individual measurements.

3 RESULTS

Based on SED fits, we estimated M_*, SFR, stellar age, $E(B-V)$ and sSFR for each galaxy. We present the distribution of these SED-modelled parameters for the KLCS SED sample in Fig. 3. The median and standard deviation of each respective measurement distribution are displayed, respectively, as dark points and error bars. In the figure, we use dashed vertical lines to indicate the edges of the three equal-sized (n = 32) samples that comprise the bins for generating composite spectra.

A composite spectrum was generated for each binned sample detailed in Fig. 3, and three estimates of ionizing-photon escape were measured, as described in Section 2.3. The first, $\langle f_{900}/f_{1500}\rangle_{\rm obs}$, is the ratio of ionizing to non-ionizing flux density directly observed in the composite generated from individual spectra. The second, $\langle f_{900}/f_{1500}\rangle_{\rm out}$, is the same ratio instead measured from a composite corrected for mean line-of-sight attenuation from the IGM and CGM. Finally, $f_{\rm esc}$ is a parameter estimated via stellar-population synthesis and ISM modeling of the full rest-UV composite. We display the

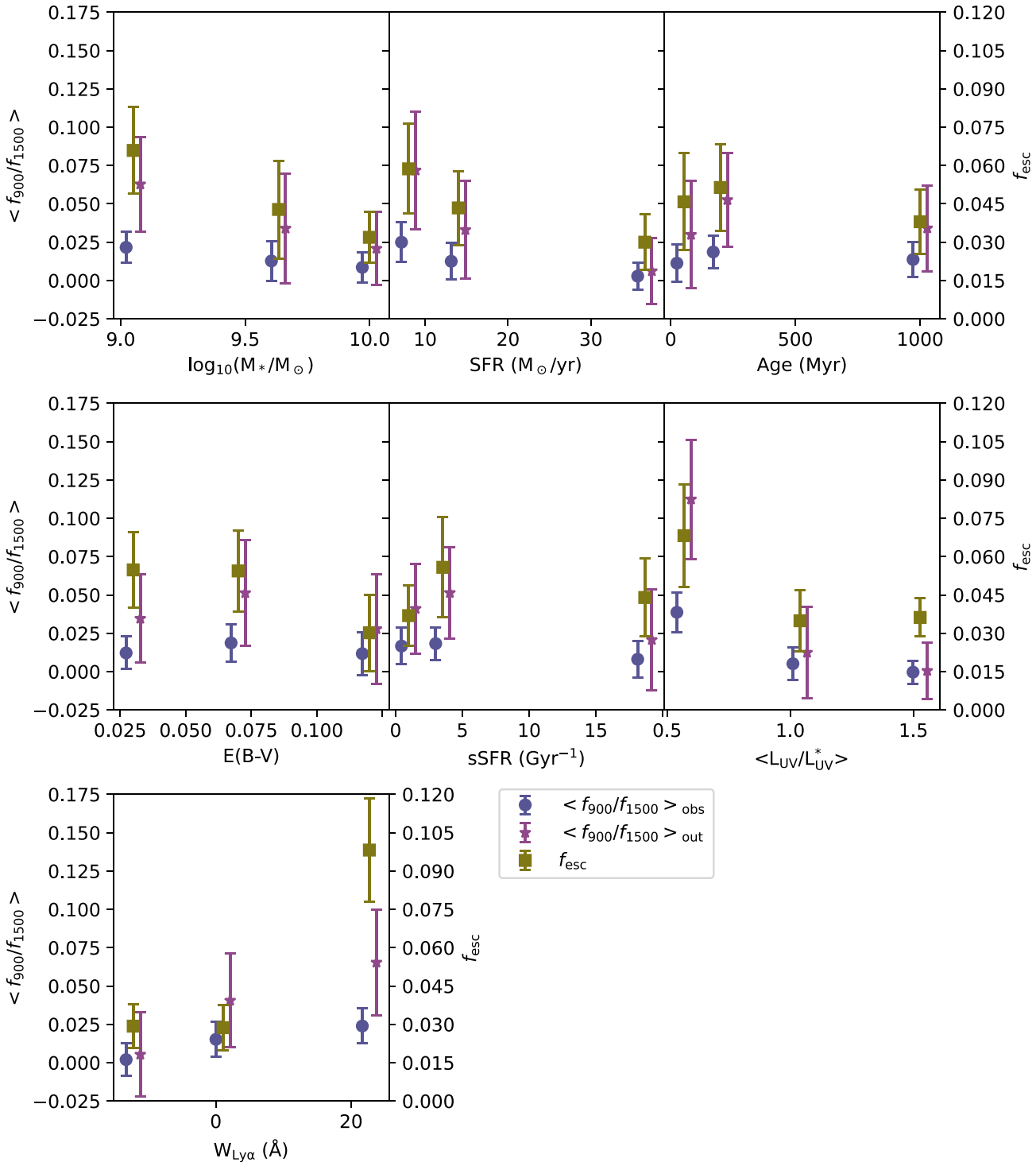

Figure 4. Different measures of ionizing escape for the KLCS SED sample binned according to several galaxy properties. Each escape parameter is presented as a function of the median of the respective galaxy property of the binned subsample. Measurements of $\langle f_{900}/f_{1500}\rangle_{obs}$ are presented as blue circles and are based on uncorrected composite spectra. Measurements of $\langle f_{900}/f_{1500}\rangle_{out}$ are presented as purple stars and are based on composite spectra corrected for attenuation of the IGM + CGM; estimates of f_{esc} are presented as yellow squares and are based on SPS model fits and modelling of the ISM according to the 'holes' model (Steidel et al. 2018; Reddy et al. 2016b, 2022). Blue circles and purple stars are shifted left and right, respectively, for visual clarity.

three measurements of ionizing escape and their respective errors for each subsample binned as a function of galaxy property in Fig. 4. These results are tabulated in Table 2, which includes the median galaxy properties of each subsample.

To determine whether ionizing-photon escape is correlated with measured galaxy properties, we define a 'significant' correlation as fulfilling two criteria: the escape parameter varies monotonically across the three bins, and the difference between the escape parameter

Table 2. Different measurements of ionizing-photon escape for the KLCS SED sample, binned according to several galaxy properties.

	$\log_{10}(M_{*,med}/M_\odot)^a$	$SFR_{med}(M_\odot yr^{-1})^a$	Age_{med} (Myr)^a	$E(B-V)_{med}{}^a$	$sSFR_{med}$ (Gyr^{-1})^a	$<L_{UV,med}/L^*_{UV}>^a$	$W_{Ly\alpha,med}$ (Å)^a	$<f_{900}/f_{1500}>_{obs}$	$<f_{900}/f_{1500}>_{out}$	f_{esc}
$M_{*,low}$	**9.05 ± 0.06**	13.0 ± 1.9	63 ± 13	0.075 ± 0.009	15.5 ± 2.5	0.71 ± 0.09	2.7 ± 5.5	0.022 ± 0.010	0.063 ± 0.031	0.07 ± 0.02
$M_{*,mid}$	**9.63 ± 0.03**	14.5 ± 4.8	251 ± 72	0.070 ± 0.011	3.9 ± 1.3	1.06 ± 0.11	1.1 ± 2.8	0.013 ± 0.013	0.034 ± 0.036	0.04 ± 0.02
$M_{*,high}$	**10.00 ± 0.09**	15.5 ± 4.4	815 ± 268	0.065 ± 0.011	1.2 ± 0.4	1.29 ± 0.13	−2.1 ± 3.3	0.009 ± 0.010	0.021 ± 0.024	0.03 ± 0.01
SFR_{low}	9.60 ± 0.11	**8.0 ± 0.5**	475 ± 169	0.050 ± 0.010	2.0 ± 0.8	0.62 ± 0.10	2.5 ± 2.5	0.025 ± 0.013	0.072 ± 0.038	0.06 ± 0.02
SFR_{mid}	9.62 ± 0.16	**14.0 ± 0.9**	316 ± 107	0.070 ± 0.009	3.1 ± 1.8	0.93 ± 0.12	−2.5 ± 4.1	0.013 ± 0.012	0.033 ± 0.032	0.04 ± 0.01
SFR_{high}	9.69 ± 0.07	**36.5 ± 4.1**	100 ± 37	0.110 ± 0.015	9.9 ± 3.3	1.32 ± 0.10	−1.2 ± 1.9	0.003 ± 0.009	0.006 ± 0.021	0.03 ± 0.01
Age_{low}	9.27 ± 0.12	19.0 ± 6.0	**53 ± 14**	0.090 ± 0.009	17.6 ± 2.7	0.96 ± 0.16	0.7 ± 4.5	0.011 ± 0.012	0.030 ± 0.035	0.05 ± 0.02
Age_{mid}	9.59 ± 0.09	15.0 ± 3.7	**199 ± 54**	0.070 ± 0.009	4.6 ± 1.4	1.02 ± 0.15	0.3 ± 3.0	0.019 ± 0.011	0.053 ± 0.031	0.05 ± 0.02
Age_{high}	9.94 ± 0.10	11.0 ± 1.9	**1000 ± 225**	0.050 ± 0.011	1.0 ± 0.2	1.08 ± 0.11	1.6 ± 2.7	0.014 ± 0.011	0.034 ± 0.028	0.04 ± 0.01
$E(B-V)_{low}$	9.70 ± 0.10	9.0 ± 0.8	501 ± 134	**0.030 ± 0.004**	1.9 ± 0.5	0.97 ± 0.08	3.8 ± 2.5	0.012 ± 0.011	0.035 ± 0.029	0.05 ± 0.01
$E(B-V)_{mid}$	9.59 ± 0.14	14.0 ± 1.2	251 ± 77	**0.070 ± 0.005**	3.9 ± 1.3	0.86 ± 0.13	1.1 ± 3.3	0.019 ± 0.012	0.051 ± 0.034	0.05 ± 0.02
$E(B-V)_{high}$	9.66 ± 0.07	33.0 ± 5.9	100 ± 24	**0.120 ± 0.011**	10.0 ± 2.6	1.18 ± 0.10	−1.8 ± 2.5	0.012 ± 0.014	0.028 ± 0.036	0.03 ± 0.01
$sSFR_{low}$	9.90 ± 0.10	10.0 ± 1.9	1000 ± 241	0.050 ± 0.010	**1.0 ± 0.2**	1.08 ± 0.11	1.6 ± 2.7	0.017 ± 0.012	0.041 ± 0.029	0.04 ± 0.01
$sSFR_{mid}$	9.63 ± 0.06	13.5 ± 3.0	284 ± 57	0.065 ± 0.009	**3.5 ± 0.7**	0.97 ± 0.14	1.0 ± 2.4	0.018 ± 0.011	0.051 ± 0.030	0.06 ± 0.02
$sSFR_{high}$	9.08 ± 0.14	22.0 ± 6.3	50 ± 4	0.090 ± 0.009	**18.7 ± 1.0**	0.98 ± 0.16	0.2 ± 5.8	0.008 ± 0.012	0.021 ± 0.033	0.04 ± 0.02
$L_{UV,low}$	9.22 ± 0.13	9.0 ± 1.1	125 ± 82	0.070 ± 0.008	7.7 ± 2.7	**0.57 ± 0.03**	2.9 ± 5.9	0.039 ± 0.013	0.112 ± 0.039	0.07 ± 0.02
$L_{UV,mid}$	9.65 ± 0.06	14.0 ± 1.4	284 ± 90	0.070 ± 0.011	3.5 ± 1.2	**1.04 ± 0.05**	2.6 ± 3.5	0.005 ± 0.011	0.012 ± 0.030	0.03 ± 0.01
$L_{UV,high}$	9.85 ± 0.07	28.0 ± 4.9	251 ± 134	0.075 ± 0.012	3.9 ± 2.1	**1.53 ± 0.04**	−2.2 ± 1.5	−0.000 ± 0.008	0.001 ± 0.018	0.04 ± 0.01
$W_{Ly\alpha,low}$	9.72 ± 0.13	14.0 ± 1.8	251 ± 111	0.080 ± 0.006	3.9 ± 2.3	1.08 ± 0.13	**−12.2 ± 1.1**	0.002 ± 0.011	0.005 ± 0.028	0.03 ± 0.01
$W_{Ly\alpha,mid}$	9.72 ± 0.09	17.2 ± 3.0	316 ± 112	0.060 ± 0.010	3.1 ± 1.7	1.32 ± 0.15	**1.1 ± 0.8**	0.015 ± 0.011	0.041 ± 0.031	0.03 ± 0.01
$W_{Ly\alpha,high}$	9.57 ± 0.13	12.5 ± 3.0	199 ± 94	0.070 ± 0.012	4.9 ± 4.2	0.84 ± 0.08	**22.7 ± 3.7**	0.024 ± 0.011	0.065 ± 0.035	0.10 ± 0.02

[a]The medians and standard error of the subsamples with respect to a given galaxy property, with the binned parameter highlighted in bold.

in the highest and lowest bins was $>1\sigma$. Using f_{esc} as an example, we define a $> 1\sigma$ difference as

$$|f_{esc,highest} - f_{esc,lowest}| > \sqrt{\left(\sigma_{f_{esc,highest}}\right)^2 + \left(\sigma_{f_{esc,lowest}}\right)^2}, \quad (1)$$

where $f_{esc,\,highest}$ is measured from the third tertile of a given galaxy property, $f_{esc,\,lowest}$ is from the first tertile, and $\sigma_{f_{esc,highest}}$ and $\sigma_{f_{esc,lowest}}$ are their corresponding errors derived as described in Section 2.3.

As seen in the upper left-hand panel of Fig. 4, both $\langle f_{900}/f_{1500}\rangle_{out}$ and f_{esc} are significantly, negatively correlated with M_* in the KLCS SED sample, such that lower mass galaxies have higher escape fractions. The two measures of LyC escape are also significantly negatively correlated with SFR, shown in the upper central panel. While we find no significant correlation with $\langle f_{900}/f_{1500}\rangle_{out}$ and $E(B-V)$, we do find a significant negative correlation with f_{esc} and $E(B-V)$, as displayed in the middle left-hand panel. Discrepancies between these two parameters of LyC escape arise from the fact that the fitting process to determine f_{esc} incorporates additional information from the composite spectrum, including the Lyman series absorption features and the UV spectral shape. Correlation between ionizing-escape parameters and $E(B-V)$ is expected in our analysis considering that neutral gas and dust are spatially associated (Reddy et al. 2016b; Du et al. 2018; Pahl et al. 2020). We also see an anticorrelation between f_{esc} and $E(B-V)$ when inferring E(B-V) from rest-UV spectral modeling. Finally, we find no significant correlation between $\langle f_{900}/f_{1500}\rangle_{out}$ or f_{esc} and stellar age or sSFR, seen in the middle left and center panels of Fig. 4, respectively. We additionally computed these trends using a modified SED fitting process that assumed a Calzetti et al. (2000) dust extinction curve, and found qualitative agreement in the trends between f_{esc} and galaxy properties, although we note that a stronger f_{esc}–$E(B-V)$ trend was recovered when using the SMC curve. We consider our SED modelling process that utilizes the SMC curve fiducial, considering greater consistency has been found between SED-fit SFR measurements and Hα-based SFRs when assuming an SMC dust extinction curve rather than Calzetti et al. (2000) at $z \sim 2$ (Reddy et al. 2022). Additionally, Reddy et al. (2018) demonstrated that $z \sim 2$ star-forming galaxies have an IRX – β relation consistent with predictions only when assuming an SMC dust curve.

We also note that f_{esc} and $\langle f_{900}/f_{1500}\rangle_{out}$ are significantly correlated with $W_\lambda(\mathrm{Ly}\,\alpha)$ and L_{UV} in this analysis, seen in the middle right-hand and bottom panels of Fig. 4, mirroring the results of the full KLCS presented in Steidel et al. (2018) and Pahl et al. (2021). The positive trend between f_{esc} and $W_\lambda(\mathrm{Ly}\,\alpha)$ has also been confirmed in additional $z \sim 3$–4 LyC surveys (Marchi et al. 2017, 2018; Fletcher et al. 2019; Begley et al. 2022). In Pahl et al. (2022), we argued that recovering these well-established spectral trends is important for determining whether a sample is sufficiently large and representative for examining relationships between f_{esc} and other galaxy properties. Considering the KLCS SED sample has both the size (n = 96) and dynamic range of galaxy properties to confidently recover trends between f_{esc} and $W_\lambda(\mathrm{Ly}\,\alpha)/L_{UV}$, we conclude that the KLCS SED sample is sufficient and representative, fulfilling the requirements for determining the trends between f_{esc} and galaxy property presented in this section. We note that if subtle correlations do exist between f_{esc} and age or sSFR, we may require a larger sample to discern these trends.

4 DISCUSSION

The connections between f_{esc} and galaxy properties at $z \sim 3$ provide key insights into the physics of ionizing-photon escape, and also indicate the most appropriate assumptions for f_{esc} at even higher redshift, during the epoch of reionization. We find that galaxies with higher f_{esc} tend to have lower $E(B-V)$, which is consistent with a physical picture in which dust is spatially coincident with neutral-phase gas in a galaxy, such that an ISM with a higher neutral-gas covering fraction will be both dustier and have lower associated f_{esc} (Reddy et al. 2016b; Du et al. 2018; Pahl et al. 2020). In addition, ionizing photons are more attenuated by dust than non-ionizing photons (Reddy et al. 2016a). We find a negative trend between both f_{esc} and $\langle f_{900}/f_{1500}\rangle_{out}$ and M_*, highlighting the fact that more massive galaxies at $z \sim 3$ have conditions that are less conducive to LyC escape. This relationship is likely due to the fact that more massive galaxies tend to be dustier (e.g. Whitaker et al. 2017; McLure et al. 2018). Finally, the lack of trend between f_{esc} and either stellar age or sSFR is in tension with the physical picture advanced in simulations that bursts of recent star formation induce favorable channels in the ISM and CGM for ionizing photons to escape (Ma et al. 2020). In this section, we introduce comparisons between our results and recent LyC surveys both at $z \sim 3$ and in the local Universe. We also connect our ionizing-photon escape trends or lack thereof with radiative transfer modelling of simulated galaxies and the predictions from reionization models.

4.1 Comparison to related observational surveys

Direct comparisons can be made between our reported trends between f_{esc} and galaxy property and those found in recent LyC surveys at $z \sim 3$. Of particular note are the recent photometric LyC measurements of 148 galaxies from the VANDELS survey at $3.35 \leq z \leq 3.95$ (Begley et al. 2022). These authors constrained the average f_{esc} of the sample as $\langle f_{esc}\rangle = 0.07 \pm 0.02$, consistent with $\langle f_{esc}\rangle = 0.06 \pm 0.01$ measured from the uncontaminated KLCS (Pahl et al. 2021). The VANDELS LyC sample was binned in two as a function of a variety of galaxy properties. A positive correlation between f_{esc} and $W_\lambda(\mathrm{Ly}\,\alpha)$ and a negative correlation between f_{esc} and L_{UV} reported in the VANDELS analysis aligns with the correlations found in the KLCS SED sample and the full KLCS (Steidel et al. 2018; Pahl et al. 2021). Best-fitting f_{esc} values were also calculated for two bins of increasing M_* in the VANDELS sample, which we display alongside our f_{esc} versus M_* measurements for the KLCS SED sample in Fig. 5. A weak anticorrelation was observed between f_{esc} and M_* in the VANDELS analysis when utilizing maximum-likelihood estimation (MLE) to determine f_{esc}, consistent with trends found using indirect measurements of f_{esc} in VANDELS (Saldana-Lopez et al. 2022a). No correlation was found when using a Bayesian estimate of f_{esc}. The trend between the VANDELS MLE f_{esc} values and M_* is remarkably consistent with our results. In addition, the reported f_{esc} values for both Bayesian and MLE methods from VANDELS are consistent with our f_{esc} constraints at comparable M_*; however, we note that the VANDELS results use modelling that more closely resembles the 'screen' model of Steidel et al. (2018), rather than the 'holes' model used in this work. Using the 'screen' model results in ~ 30 per cent higher $\langle f_{esc}\rangle$ than using the 'holes' model in the KLCS (Steidel et al. 2018), which is still consistent with the VANDELS results. The VANDELS analysis also recovered a significant anticorrelation between f_{esc} and UV dust attenuation, where dust attenuation was quantified in terms of the UV slope, β. These results are qualitatively consistent with the anticorrelation between f_{esc} and $E(B-V)$ we present in the central left-hand panel of Fig. 4.

Stellar population parameters have also been explicitly correlated with $W_\lambda(\mathrm{Ly}\,\alpha)$ in galaxy surveys at $z \sim 2$–5. These trends are informative for interpreting LyC escape considering that the strength

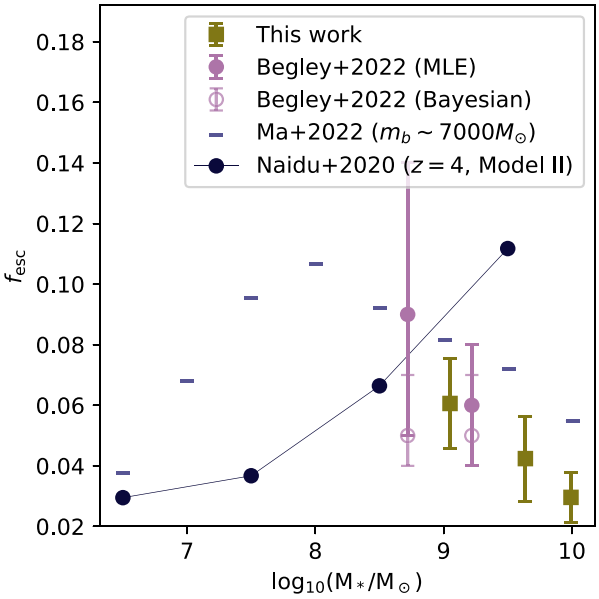

Figure 5. Inferred f_{esc} as a function of stellar mass from this work alongside trends from observation and modelling. Estimates of f_{esc} for three bins of increasing M_* for the KLCS SED sample are presented as yellow boxes, and are identical to values presented in Fig. 4. The f_{esc} constraints from two bins of increasing M_* from 148 $z \sim 3.5$ galaxies from VANDELS (Begley et al. 2022) are displayed as purple circles. Solid, purple circles represent f_{esc} fit by maximum-likelihood analysis, while skeletal purple circles represent f_{esc} fit by Bayesian analysis. Predictions for f_{esc} from the FIRE-2 cosmological simulations at a particle mass of $m_B \sim 7000\,M_\odot$ are displayed as horizontal bars (Ma et al. 2020). Predicted f_{esc} as a function of M_* at $z \sim 4$ for the fiducial model of Naidu et al. (2020) are displayed as dark circles.

of Ly α emission is similarly modulated by the neutral gas covering fraction (e.g. Steidel et al. 2010, 2011, 2018; Verhamme et al. 2015; Reddy et al. 2016b). Stacks of rest-UV spectra at $z \sim 2$–5 have demonstrated anticorrelations between W_λ(Ly α) and both M_* and SFR (Du et al. 2018; Pahl et al. 2020), mimicking the anticorrelations between f_{esc} and these parameters that we presented in Fig. 4. Meanwhile, surveys at this redshift have shown either no strong correlation between W_λ(Ly α) and age (Du et al. 2018; Pahl et al. 2020) or only a weak correlation (Reddy et al. 2022). These analyses of Ly α escape in combination with our f_{esc} trends indicate that stellar age may not as closely linked to the configuration of neutral-phase gas in the ISM and CGM of a galaxy as much as other galaxy properties, such as M_*, L_{UV}, $E(B-V)$, and SFR.

While the $z \sim 3$–4 Universe is an excellent laboratory to test LyC escape physics in galactic environments more similar to those at $z > 6$, LyC surveys in the local Universe are afforded advantages such as the ability to examine the direct ionizing signals from intrinsically fainter galaxies in the dwarf galaxy regime, which may dominate the ionizing background during the epoch of reionization (Robertson et al. 2015; Finkelstein et al. 2019). In addition, local surveys avoid the sightline variability of the IGM that necessitates binning at $z \sim 3$ (Steidel et al. 2018), enabling constraints on f_{esc} for individual objects.

The Low-redshift Lyman Continuum Survey (LzLCS) analysed 66 galaxies at $z = 0.2$–0.4 observed with the *HST*/COS, and reported 35 galaxies individually detected in LyC (Flury et al. 2022a, b). The galaxies were indirectly selected to be strongly leaking using [O III]λ5007/[O II]$\lambda\lambda$3726, 3729, SFR surface density, and UV spectral slope, in contrast the LBG-selected KLCS. The correlation between a number of galaxy properties and f_{esc} were considered, where f_{esc} was inferred from stellar-population synthesis fits to COS UV spectra, similar to our determinations of f_{esc} for the KLCS SED sample. The LzLCS f_{esc} values appear to decrease as a function of increasing M_*, consistent with the negative trend, we present in the upper left-hand panel of Fig. 4. However, the correlation coefficient between f_{esc} and M_* was determined not to be significant, mirroring other local explorations of the two variables (Izotov et al. 2021). Augmenting this result, an examination of the LzLCS sample in tandem with archival observations (totaling 89 star-forming galaxies at $z \sim 0.3$) found that galaxies at lower M_* tend to have both bluer spectral slopes and higher f_{esc} (Chisholm et al. 2022). This analysis focused on the strong inverse correlation found between f_{esc} and the UV spectral slope at 1550 Å (β_{1500}) in the expanded sample. While UV spectral slope can encapsulate both the intrinsic spectral slope of the stellar population and the degree of dust reddening in the UV, β_{1500} was strongly correlated with $E(B-V)$ and uncorrelated with stellar age, indicating that β_{1500} for the LzLCS is primarily reflecting the degree of dust reddening (also see Saldana-Lopez et al. 2022b). Apparent anticorrelations between f_{esc} and β_{1500} are supported by our anticorrelation of f_{esc} and E(B-V) seen in the center left panel of Fig. 4. None the less, Chisholm et al. (2022) make predictions for f_{esc} vs. M_{UV} at $z \sim 3$ that are too low when compared to the $\langle f_{esc} \rangle = 0.06 \pm 0.01$ of the KLCS (at $M_{UV} \sim -21$), despite reproducing our qualitative relationship between f_{esc} and L_{UV} shown in the center right-hand panel of Fig. 4.

A weaker, but still significant trend of f_{esc} and sSFR was also observed in the LzLCS, contrasting with the lack of trend between f_{esc} and sSFR that we presented in the central panel of Fig. 4. We note that the LzLCS modelling allows for arbitrarily-short stellar ages, in contrast with our SED fitting procedure, which ensures ages are greater than typical dynamical time-scales (50 Myr). Finally, f_{esc} is strongly correlated with W_λ(Ly α) in the LzLCS analysis, which is broadly consistent with the correlation found for both the KLCS SED sample in Fig. 4 and the full KLCS in Steidel et al. (2018) and Pahl et al. (2021).

We also note that strong correlations are found between f_{esc} and Ly α peak separation (v_{sep}) and star-formation rate surface density (Σ_{SFR}) in the LzLCS. These potential tracers of f_{esc} remain unconfirmed at $z \sim 3$, and, in particular, the number of galaxies with *HST* imaging in the KLCS remains insufficient for testing the connection between f_{esc} and Σ_{SFR} (Pahl et al. 2022). However, future work will examine potential connections between f_{esc} and v_{sep} at $z \sim 3$ by leveraging higher-resolution spectroscopy of the Ly α profiles of KLCS galaxies and f_{esc} and Σ_{SFR} in the VANDELS survey.

4.2 Comparison to models

Theoretical predictions for f_{esc} in a variety of galactic environments can help elucidate fundamental relationships between galactic physics and escaping ionizing radiation in the earliest galaxy populations, where direct LyC detections are impossible. The feedback in realistic environments (FIRE-2; Hopkins et al. 2018) project was coupled with radiative transfer in post-processing to examine f_{esc} in cosmological zoom-in simulations of galaxies, evolved down to $z = 5$ (Ma et al. 2020). An increase of f_{esc} with increasing mass was found up to $\log(M_*/M_\odot) \sim 8$, and a subsequent decrease in f_{esc} was found at $\log(M_*/M_\odot) > 8$. The increasing relationship between f_{esc} and M_* was determined to be due to an increasing efficiency of star formation and feedback, while the decrease at the high-mass end can be explained by increasing dust attenuation. We display this trend as dark horizontal bars in Fig. 5, specifying the simulation

resolution that extends to the stellar masses of our sample (baryonic particle mass $m_b \sim 7000\,M_\odot$). The negative trend between f_{esc} and M_* at $\log(M_*/M_\odot) > 8$ found in Ma et al. (2020) is consistent with the negative trend we find in the KLCS SED sample, which has a median $\log(M_*/M_\odot) = 9.6$. We do find overall lower f_{esc} values than the FIRE-2 results at fixed M_*. This discrepancy may be expected considering higher f_{esc} values were found with increasing redshift at fixed M_* in the simulated galaxies.

Evidence of a turnover in the relationship between f_{esc} and M_* was also found in Kostyuk et al. (2022), which utilized the IllustrisTNG (Marinacci et al. 2018; Naiman et al. 2018; Nelson et al. 2018, 2019; Pillepich et al. 2018; Springel et al. 2018) cosmological simulations coupled with the radiative transfer code CRASH (Graziani, Maselli & Ciardi 2013). These authors also found significant scatter in the relationship between f_{esc} and M_*, due to both differences in ionizing photon production rates and the distribution of stars within the neutral ISM. The SPHINX simulations have also similarly reported this relationship, finding a f_{esc} trend that peaks at $\log(M_*/M_\odot) \sim 7$ and drops off strongly at lower and higher masses (Rosdahl et al. 2022).

Finally, Ma et al. (2020) also explored potential synchronization of periods of intense star formation and elevated f_{esc} values. They find that feedback from star formation clears sightlines in the ISM and CGM of a galaxy, creating favourable conditions for ionizing photons to escape. This process leads to a correlation between a burst of star-formation and high f_{esc}, albeit with a few Myr time delay. If true, one might expect a higher f_{esc} in galaxies with shorter stellar ages and elevated sSFR. We find no correlation between f_{esc} and these two properties in the KLCS SED analysis, as shown in Fig. 4. The absence of an observed trend could be explained by a less bursty SFH than those found in Ma et al. (2020), which would reduce potential dependencies between f_{esc} and stellar age.

4.3 Implications for reionization

Models of reionization and their predicted timelines are built upon assumptions regarding f_{esc}, which are impossible to constrain directly in the reionization era. Some assume single values of f_{esc} for all galaxies for simplicity (typically 10–20 per cent; Robertson et al. 2015; Ishigaki et al. 2018), others assume that f_{esc} depends on halo mass (Finkelstein et al. 2019), or that f_{esc} depends on one particular galaxy property (Naidu et al. 2020; Matthee et al. 2022).

We compare our f_{esc} versus M_* trend to the predictions of the fiducial model of Naidu et al. (2020), which concludes that reionization is 'oligarchical,' such that the most luminous, massive [$M_{UV} < -18$ and $\log(M_*/M_\odot) > 8$] galaxies at $z > 6$ contribute the bulk of the ionizing photon budget. In this model, a direct relationship between f_{esc} and Σ_{SFR} is assumed such that $f_{esc} = 1.6 \times \Sigma_{SFR}^{0.4}$. As massive and UV bright galaxies tend to have high Σ_{SFR}, the assumed connection between f_{esc} and Σ_{SFR} results in a positive relationship between f_{esc} and M_*. We display this trend determined at $z = 4$ as dark circles in Fig. 5. The trend we observe between f_{esc} and M_* at $z \sim 3$ is inconsistent with the direction and magnitude of the model curve within the mass range where the model and observations overlap. Specifically, we show that f_{esc} decreases with increasing M_* at $\log(M_*/M_\odot) \sim 9.5$. We also find significantly lower $\langle f_{esc} \rangle$ at fixed M_* than is predicted by the model. Some of this offset at fixed mass is likely due to the average value of $\langle f_{esc} \rangle = 0.09 \pm 0.01$ from Steidel et al. (2018), used as a constraint in the model, considering $\langle f_{esc} \rangle$ of the KLCS was corrected to $\langle f_{esc} \rangle = 0.06 \pm 0.01$ after removal of foreground contamination (Pahl et al. 2021). Additionally, the fiducial model of Naidu et al. (2020) does not explicitly consider dust, which we find is a significant factor modulating the escape fraction of galaxies in our sample. To conservatively match observed relationships between f_{esc} and M_* at $z \sim 3$, assumed f_{esc} values of galaxies at $M_* > 10^9\,M_\odot$ should be no higher than the f_{esc} values of $M_* \sim 10^{8.5}\,M_\odot$ galaxies. Specifically, the f_{esc} value for the most massive M_* data point from Naidu et al. (2020) should shift to become lower than or equal to the f_{esc} value for the second-most-massive data point. Meeting this requirement at $z \sim 4$, which is the closest point of contact between the Naidu et al. (2020) model and our observations, would require a reduction in f_{esc} for $M_* > 10^9$ galaxies by a factor of two in the fiducial model of Naidu et al. (2020). Satisfying this criterion at $z > 6$ during the epoch of reionization would require a similar reduction. This adjustment would significantly shift the burden of reionization to lower mass galaxies (e.g. Finkelstein et al. 2019).

The rapidity of reionization depends strongly on the population of galaxies that dominates the ionizing emissivity over cosmic time. Our results indicate that fainter, less massive galaxies with lower dust content have conditions favourable for escaping ionizing radiation, broadly consistent with other recent LyC observations at $z \sim 3$ (Begley et al. 2022) and in the local Universe (Flury et al. 2022a, b; Chisholm et al. 2022). If these trends were present within the epoch of reionization, the process of reionization may have started early and progressed gradually, such that the IGM neutral fraction is 20 per cent at $z \sim 7$ (Finkelstein et al. 2019), in slight tension with neutral fraction constraints from Ly α damping wing measurements (Bolton et al. 2011; Greig et al. 2017; Bañados et al. 2018). Chisholm et al. (2022) calculate the ionizing emissivity between $z \sim 4$–8 using empirical relations between f_{esc} and β_{1500} found in the LzLCS, which are consistent with our results connecting f_{esc} and $E(B-V)$, and match constraints indicating that the ionizing emissivity flattens out at $z < 5.5$ (Becker & Bolton 2013; Becker et al. 2021). However, as noted in Section 4.1, average f_{esc} values assumed by Chisholm et al. (2022) are too low at $z \sim 3$ when compared to the KLCS. As an alternative scenario, Matthee et al. (2022) instead directly tie f_{esc} to the strength of Ly α emission and build a model that produces rapid reionization and a flattened evolution of the ionizing emissivity at $z < 6$. Predicted trends between f_{esc} and L_{UV} from the model of Matthee et al. (2022) qualitatively match the KLCS anticorrelation, but underpredict the average f_{esc} at $z \sim 3$. None the less, such a prescription is promising considering that the relationship between f_{esc} and W_λ(Ly α) appears to be one of the most fundamental in our analysis. The Matthee et al. (2022) model assumes $f_{esc} = 50$ per cent for half of Ly α emitters with $L_{Ly\alpha} > 10^{42}$ erg s^{-1}, based on the Ly α line profile shapes of $z \sim 2$ Ly α emitters (Naidu et al. 2022). Our ongoing spectroscopic observing program to explore the connection between Ly α profile shape and LyC escape in the KLCS will test this formalism, which relies on a correlation between f_{esc} and Ly α peak separation that currently lacks direct observational support at high redshift.

Both the Chisholm et al. (2022) and Matthee et al. (2022) models highlight important existing relationships found between f_{esc} and galaxy property in our analyses, and present ionizing emissivities that both overcome recombination in the IGM at $z \sim 8$ and avoid overproducing ionizing photons at $z < 6$. The trends between f_{esc} and galaxy properties presented in this work are vital for anchoring assumptions of f_{esc} during the epoch of reionization, where direct constraints on f_{esc} are impossible. Future reionization models can utilize these relationships to ensure consistency between reionization-era f_{esc} prescriptions and our empirical results, particularly in comparable galaxy populations that have similar luminosities and masses to those of our sample. We will extend our analysis of f_{esc} and galaxy properties to lower L_{UV} in future work, which will elucidate most

fundamental predictors of f_{esc} for a larger dynamic range of galaxy properties.

5 SUMMARY

In this work, we examine the underlying processes behind the escape of ionizing radiation by exploring trends between f_{esc} and galaxy properties at $z \sim 3$. We accomplish this goal by leveraging multiband photometry of galaxies observed spectroscopically as part of KLCS. We examined a subsample of 96 KLCS galaxies with photometry suitable for SED fitting, and determined galaxy population parameters of M_*, SFR, sSFR, $E(B-V)$, and age from these stellar-population synthesis fits. For each galaxy property, we sorted the 96 galaxies and divided them into three equal-sized bins, constructing a rest-UV composite spectrum for each bin. The main results regarding the estimated Lyman-continuum escape parameters of $\langle f_{900}/f_{1500}\rangle_{out}$ and f_{esc} and their relationships with galaxy properties are as follows:

(i) We find significant correlations between f_{esc} and $W_\lambda(\mathrm{Ly}\,\alpha)$ and anticorrelations between f_{esc} and L_{UV} in the KLCS SED subsample, indicating that our sample is representative of the full KLCS and appropriate for constraining f_{esc} as a function of other galaxy properties (Pahl et al. 2022).

(ii) We find significant anticorrelation between f_{esc} and $E(B-V)$ across three bins of increasing $E(B-V)$, although no correlation between $\langle f_{900}/f_{1500}\rangle_{out}$ and $E(B-V)$. The f_{esc} result indicates that dust modulates escaping ionizing radiation at $z \sim 3$. Such modulation naturally arises due to the spatial coincidence of neutral-phase gas and dust (Reddy et al. 2016b; Du et al. 2018; Pahl et al. 2020), and the fact that dust directly absorbs LyC photons (Reddy et al. 2016a). These results are broadly consistent with anticorrelations found between f_{esc} and UV spectral slope at $z \sim 3.5$ (Begley et al. 2022) and in the local Universe (Flury et al. 2022a, b; Chisholm et al. 2022).

(iii) Both $\langle f_{900}/f_{1500}\rangle_{out}$ and f_{esc} are significantly correlated with M_* and SFR. Trends between f_{esc} and M_* have also been suggested in other LyC surveys at high and low redshift (Begley et al. 2022; Flury et al. 2022a, b). The sense of the relationships we observe is consistent with recovered anticorrelation between f_{esc} and M_* for $\log(M_*/M_\odot) > 8$ galaxies in cosmological simulations (Ma et al. 2020; Kostyuk et al. 2022).

(iv) Some cosmological zoom-in simulations of reionization-era galaxies connect stellar feedback and favorable ISM/CGM conditions for LyC escape (e.g. Ma et al. 2020), which would plausibly manifest as elevated estimates of f_{esc} in galaxies with shorter inferred stellar ages and higher sSFR. However, we find no correlation between $\langle f_{900}/f_{1500}\rangle_{out}$ or f_{esc} and stellar age or sSFR, providing no direct observational support for the synchronization of recent bursts of star formation and the escape of ionizing photons at these masses. These trends are consistent with the absent or weak correlation found between $W_\lambda(\mathrm{Ly}\,\alpha)$ and stellar age in earlier work (Du et al. 2018; Pahl et al. 2020; Reddy et al. 2022).

These results represent a comprehensive exploration of f_{esc} and SED-modelled properties at high redshift, grounding assumptions of f_{esc} for galaxies in the reionization era. Significant unknowns still remain for f_{esc} and its dependencies in galaxies less luminous than those in our sample, particularly at $z \sim 3$. In future work, we will extend our examination of f_{esc} and galaxy properties down to lower UV luminosities. Additional indirect diagnostics of f_{esc} that have proven promising in the local Universe can also be tested at high redshift with the KLCS. Ongoing follow-up of the Ly α line profiles of KLCS galaxies will elucidate potential trends between f_{esc} and Ly α peak separation, and Keck/MOSFIRE spectra in hand for a substantial subset of the KLCS will enable an examination of the relationships between nebular emission-line properties and f_{esc}. Using the results summarized in this section in tandem with future analyses of the KLCS, we will attempt to offer a unified picture of escaping ionizing radiation at $z \sim 3$. This picture is vital for understanding the contribution of star-forming galaxies to reionization at earlier times.

ACKNOWLEDGEMENTS

We acknowledge support from NSF AAG grants 0606912, 0908805, 1313472, 2009313, 2009085, and 2009278. Support for program HST-GO-15287.001 was provided by NASA through a grant from the Space Telescope Science Institute, which is operated by the Associations of Universities for Research in Astronomy, Incorporated, under NASA contract NAS5-26555. CS was supported in part by the Caltech/JPL President's and Director's program. Based in part on observations obtained with MegaPrime/MegaCam, a joint project of CFHT and CEA/IRFU, at the Canada–France–Hawaii Telescope (CFHT) which is operated by the National Research Council (NRC) of Canada, the Institut National des Science de l'Univers of the Centre National de la Recherche Scientifique (CNRS) of France, and the University of Hawaii. This work is based in part on data products produced at Terapix available at the Canadian Astronomy Data Centre as part of the Canada–France–Hawaii Telescope Legacy Survey, a collaborative project of NRC and CNRS. This paper includes data gathered with the 6.5 m Magellan Telescopes located at Las Campanas Observatory, Chile. We thank D. Kelson for the use of his FourCLift FourStar Reduction code and for his assistance with it. We wish to extend special thanks to those of Hawaiian ancestry on whose sacred mountain, we are privileged to be guests. Without their generous hospitality, most of the observations presented herein would not have been possible.

DATA AVAILABILITY

The *HST* data referenced in this article are publicly available from the Mikulski Archive for Space Telescopes. The ground-based data presented here will be shared on reasonable request to the corresponding author.

REFERENCES

Bañados E. et al., 2018, Nature, 553, 473
Becker G. D., Bolton J. S., 2013, MNRAS, 436, 1023
Becker G. D., D'Aloisio A., Christenson H. M., Zhu Y., Worseck G., Bolton J. S., 2021, MNRAS, 508, 1853
Begley R. et al., 2022, MNRAS, 513, 3510
Bertin E., Arnouts S., 1996, A&AS, 117, 393
Bielby R. et al., 2012, A&A, 545, A23
Bolton J. S., Haehnelt M. G., Warren S. J., Hewett P. C., Mortlock D. J., Venemans B. P., McMahon R. G., Simpson C., 2011, MNRAS, 416, L70
Bouwens R. J., Illingworth G. D., Oesch P. A., Caruana J., Holwerda B., Smit R., Wilkins S., 2015, ApJ, 811, 18
Calzetti D., Armus L., Bohlin R. C., Kinney A. L., Koornneef J., Storchi-Bergmann T., 2000, ApJ, 533, 682
Chabrier G., 2003, PASP, 115, 763
Chen Y. et al., 2021, MNRAS, 508, 19
Chisholm J. et al., 2022, MNRAS, 517, 5104
Domínguez A., Siana B., Brooks A. M., Christensen C. R., Bruzual G., Stark D. P., Alavi A., 2015, MNRAS, 451, 839

Du X. et al., 2018, ApJ, 860, 75
Eldridge J. J., Stanway E. R., Xiao L., McClelland L. A., Taylor G., Ng M., Greis S. M., Bray J. C., 2017, PASP, 34, 61
Fan X., Carilli C. L., Keating B., 2006, AR&A, 44, 415
Finkelstein S. L. et al., 2019, ApJ, 879, 36
Fletcher T. J., Tang M., Robertson B. E., Nakajima K., Ellis R. S., Stark D. P., Inoue A., 2019, ApJ, 878, 87
Flury S. R. et al., 2022a, ApJS, 260, 1
Flury S. R. et al., 2022b, ApJ, 930, 126
Gazagnes S., Chisholm J., Schaerer D., Verhamme A., Izotov Y., 2020, A&A, 639, A85
Gordon K. D., Clayton G. C., Misselt K. A., Landolt A. U., Wolff M. J., 2003, ApJ, 594, 279
Graziani L., Maselli A., Ciardi B., 2013, MNRAS, 431, 722
Greig B., Mesinger A., Haiman Z., Simcoe R. A., 2017, MNRAS, 466, 4239
Hopkins P. F. et al., 2018, MNRAS, 480, 800
Ishigaki M., Kawamata R., Ouchi M., Oguri M., Shimasaku K., Ono Y., 2018, ApJ, 854, 73
Izotov Y. I., Worseck G., Schaerer D., Guseva N. G., Chisholm J., Thuan T. X., Fricke K. J., Verhamme A., 2021, MNRAS, 503, 1734
Kostyuk I., Nelson D., Ciardi B., Glatzle M., Pillepich A., 2023, MNRAS, stad677
Law D. R., Steidel C. C., Shapley A. E., Nagy S. R., Reddy N. A., Erb D. K., 2012, ApJ, 745, 85
Ma X., Quataert E., Wetzel A., Hopkins P. F., Faucher-Giguère C. A., Kereš D., 2020, MNRAS, 498, 2001
Madau P., Dickinson M., 2014, AR&A, 52, 415
Marchi F. et al., 2017, A&A, 601, 73
Marchi F. et al., 2018, A&A, 614, 11
Marinacci F. et al., 2018, MNRAS, 480, 5113
Matthee J. et al., 2022, MNRAS, 512, 5960
McLure R. J. et al., 2018, MNRAS, 476, 3991
Mostardi R. E., Shapley A. E., Steidel C. C., Trainor R. F., Reddy N. A., Siana B., 2015, Astrophysical Journal, 810, 107
Naidu R. P., Tacchella S., Mason C. A., Bose S., Oesch P. A., Conroy C., 2020, ApJ, 892, 109
Naidu R. P. et al., 2022, MNRAS, 510, 4582
Naiman J. P. et al., 2018, MNRAS, 477, 1206
Nelson D. et al., 2018, MNRAS, 475, 624
Nelson D. et al., 2019, MNRAS, 490, 3234
Oke J. B., Gunn J. E., 1983, ApJ, 266, 713
Oke J. B. et al., 1995, PASP, 107, 375
Pahl A. J., Shapley A., Faisst A. L., Capak P. L., Du X., Reddy N. A., Laursen P., Topping M. W., 2020, MNRAS, 493, 3194
Pahl A. J., Shapley A., Steidel C. C., Chen Y., Reddy N. A., 2021, MNRAS, 505, 2447
Pahl A. J., Shapley A., Steidel C. C., Reddy N. A., Chen Y., 2022, MNRAS, 516, 2062
Parsa S., Dunlop J. S., McLure R. J., 2018, MNRAS, 474, 2904
Pillepich A. et al., 2018, MNRAS, 475, 648
Reddy N. A., Pettini M., Steidel C. C., Shapley A. E., Erb D. K., Law D. R., 2012, ApJ, 754, 31
Reddy N. A., Steidel C. C., Pettini M., Bogosavljević M., 2016a, ApJ, 828, 107
Reddy N. A., Steidel C. C., Pettini M., Bogosavljević M., Shapley A. E., 2016b, ApJ, 828, 108
Reddy N. A. et al., 2018, ApJ, 853, 56
Reddy N. A. et al., 2022, ApJ, 926, 31
Robertson B. E., Ellis R. S., Furlanetto S. R., Dunlop J. S., 2015, ApJ, 802, L19
Rosdahl J. et al., 2022, MNRAS, 515, 2386
Rudie G. C. et al., 2012, ApJ, 750, 67
Rudie G. C., Steidel C. C., Shapley A. E., Pettini M., 2013, ApJ, 769, 146
Saldana-Lopez A. et al., 2022a, The VANDELS Survey: The Ionizing Properties of Star-Forming Galaxies at 3<= Z< = 5 Using Deep Rest-Frame Ultraviolet Spectroscopy,arXiv:2211.01351
Saldana-Lopez A. et al., 2022b, A&A, 663, A59
Shapley A. E., Steidel C. C., Adelberger K. L., Dickinson M., Giavalisco M., Pettini M., 2001, ApJ, 562, 95
Shapley A. E., Steidel C. C., Strom A. L., Bogosavljević M., Reddy N. A., Siana B., Mostardi R. E., Rudie G. C., 2016, ApJ, 826, L24
Springel V. et al., 2018, MNRAS, 475, 676
Stark D. P. et al., 2015, MNRAS, 454, 1393
Stark D. P. et al., 2017, MNRAS, 464, 469
Steidel C. C., Adelberger K. L., Shapley A. E., Pettini M., Dickinson M., Giavalisco M., 2003, ApJ, 592, 728
Steidel C. C., Shapley A. E., Pettini M., Adelberger K. L., Erb D. K., Reddy N. A., Hunt M. P., 2004, ApJ, 604, 534
Steidel C. C., Erb D. K., Shapley A. E., Pettini M., Reddy N., Bogosavljević M., Rudie G. C., Rakic O., 2010, ApJ, 717, 289
Steidel C. C., Bogosavljević M., Shapley A. E., Kollmeier J. A., Reddy N. A., Erb D. K., Pettini M., 2011, ApJ, 736, 160
Steidel C. C., Bogosavljević M., Shapley A. E., Reddy N. A., Rudie G. C., Pettini M., Trainor R. F., Strom A. L., 2018, ApJ, 869, 123
Vanzella E. et al., 2012, ApJ, 751, 70
Verhamme A., Orlitová I., Schaerer D., Hayes M., 2015, A&A, 578, A7
Whitaker K. E., Pope A., Cybulski R., Casey C. M., Popping G., Yun M. S., 2017, ApJ, 850, 208
Zackrisson E., Inoue A. K., Jensen H., 2013, ApJ, 777, 39

This paper has been typeset from a TEX/LATEX file prepared by the author.